JOURNAL OF AEROSPACE INFORMATION SYSTEMS
Vol. 22, No. 8, August 2025

Spacecraft Backsubstitution Dynamics with General Multibody Prescribed Subcomponents

Leah Kiner* and Hanspeter Schaub†
University of Colorado Boulder, Boulder, Colorado 80309-0431
and
Cody Allard‡
Laboratory for Atmospheric and Space Physics, Boulder, Colorado 80303

https://doi.org/10.2514/1.I011491

In the early stages of spacecraft missions, emerging performance requirements must be rapidly verified through extensive simulation and subsequent analysis. With missions employing complex time-varying spacecraft structures, there is a marked need for flexible, scalable, and modular simulation software tools to model the effects of diverse types of multibody spacecraft dynamics. Prior work using the spacecraft dynamics backsubstitution method is expanded to consider a spacecraft consisting of a rigid hub and N six-degree-of-freedom rigid subcomponents following hub-relative prescribed motion. Unlike the original backsubstitution formulation, the kinematics of the subcomponents are prescribed, thus reducing the number of differential equations that must be solved from $6(N+1)$ to 6. Further, the new formulation permits branching and both open and closed chains in the spacecraft configuration space that were not feasible before. The solution is modular in that the dynamic impact of the subcomponents is solved generally, enabling both hub-relative translation and rotation without constraints. The Basilisk astrodynamics simulation framework is used to demonstrate an efficient, modular implementation and verify the derived dynamics. A prescribed motion solar array deployment scenario demonstrating the scalability of the derived dynamics is simulated, and the sensitivity of the hub dynamics to the deployment is investigated.

Nomenclature

B_c, F_c	=	rigid hub and prescribed body center of mass location, respectively
$\{\hat{\boldsymbol{b}}_1, \hat{\boldsymbol{b}}_2, \hat{\boldsymbol{b}}_3\}$	=	hub body frame basis vectors
$\boldsymbol{c}$	=	vector from point B to center of mass of the spacecraft C, m
$\boldsymbol{F}_{\text{ext}}$	=	vector sum of external forces on spacecraft, N
$\{\hat{\boldsymbol{f}}_1, \hat{\boldsymbol{f}}_2, \hat{\boldsymbol{f}}_3\}$	=	prescribed body frame basis vectors
$[I_{\text{sc},B}], [I_{p,F}]$	=	inertia tensor of spacecraft about point B and of prescribed body about point F, kg $\cdot$ m^2
$\boldsymbol{L}_B$	=	vector sum of external torques of spacecraft about point B, N $\cdot$ m
$m_{\text{sc}}, m_{\text{hub}}, m_P$	=	mass of spacecraft, hub, and prescribed body, respectively, kg
N, B, F	=	inertial frame origin, body frame origin, and prescribed body frame origin, respectively
$\mathcal{N}, \mathcal{B}, \mathcal{F}$	=	reference frame of inertial, hub body, and prescribed body, respectively
$\{\hat{\boldsymbol{n}}_1, \hat{\boldsymbol{n}}_2, \hat{\boldsymbol{n}}_3\}$	=	inertial frame basis vectors
$\boldsymbol{r}_{B/N}$	=	position vector of point B with respect to point N, m
$\boldsymbol{\omega}_{\mathcal{B}/\mathcal{N}}$	=	angular velocity vector of $\mathcal{B}$ frame with respect to $\mathcal{N}$ frame, deg/s

Received 6 June 2024; accepted for publication 2 May 2025; published online 12 June 2025.

*Graduate Research Assistant, Ann and H. J. Smead Department of Aerospace Engineering Sciences, 431 UCB, Colorado Center For Astrodynamics Research; leah.kiner@colorado.edu. Student Member AIAA.

†Distinguished Professor and Department Chair, Schaden Leadership Chair, Ann and H. J. Smead Department of Aerospace Engineering Sciences, 431 UCB, Colorado Center for Astrodynamics Research. Fellow AIAA.

‡Guidance, Navigation and Control Engineer, Laboratory for Atmospheric and Space Physics, 1234 Innovation Drive; cody.allard@lasp.colorado.edu.

I. Introduction

EFFECTIVE modeling and simulation of complex spacecraft concepts is crucial for the success of space missions. Particularly in the early phases of mission design, the ability to rapidly simulate a wide range of spacecraft configurations is paramount for analyzing and verifying mission requirements. Moreover, as mission concepts evolve and their objectives become more ambitious, the spacecraft designs required to fulfill the goals of such missions also grow in complexity. Among these advancements are deployment concepts and in-flight reconfigurable structures. For example, the desire to send humans into space for extended periods of time drove advancements required for space orbiters, including the Space Shuttle orbiter and the International Space Station, where multi-link robotic arms such as the Canadarm [1,2] were developed to aid in complex orbital servicing and docking operations. The latest missions to the farthest edges of our solar system have required critical component advancements in order to navigate spacecraft through deep space efficiently. The Lucy mission to the Trojan asteroids, the Emirates Mission to the Asteroid Belt (EMA), and the Double Asteroid Redirection Test (DART) binary asteroid impact mission all feature extensive solar-powered advancements to meet higher power needs. The Lucy and EMA missions use two large circular flexible-substrate solar arrays that deploy using a rotational motor-driven lanyard and articulate to track the sun [3–6]. The DART spacecraft's two rectangular Roll-Out Solar Arrays (ROSA) were the first to deploy using a roll-out method [3]. Further, in order to meet thrust vector alignment requirements for deep-space missions such as EMA, Deep Space 1 [7], Dawn [8], and Psyche [9], spacecraft ionic thruster designs advanced from hub-fixed configurations to being mounted on gimbaled platforms [6,10–12].

The field of multibody dynamics has been widely studied for several decades [13–18]. Simulating complex multibody spacecraft systems requires deriving and implementing the system's equations of motion in software. This process becomes especially challenging during mission planning when the spacecraft consists of numerous actuating components and its design is not finalized. The most effective simulation capability is achieved using a generalized dynamics formulation in software, enabling the simulation of various spacecraft configurations using a general set of motion equations. Development of these equations typically requires knowledge

of the spacecraft hub dynamics. The hub is the central, rigid core component of the spacecraft onto which solar panels, antenna, etc., are attached. The hub is usually the primary body of interest when the entire spacecraft system is simulated in a mission scenario, as it contains the science sensors, rate gyro and star trackers. Using the hub as a base of reference, the states of the other spacecraft components are described relative to the spacecraft hub-fixed frame for a consistent dynamics analysis [19,20]. The states of the spacecraft hub are tracked in simulation software and are used to evaluate attitude control and other performance requirements. Additional equations of motion for each degree of freedom contributed by the other spacecraft components must also be derived and integrated. As more components are added to the spacecraft, the computational load for numerical integration increases and the software implementation becomes cumbersome and difficult to organize.

The backsubstitution method [21–23] is a spacecraft dynamics formulation that has been recently developed to address the issues of spacecraft simulation computational efficiency, modularity, and scalability. By exploiting hub-centric spacecraft configurations and considering all dynamic components (solar panels, reaction wheels, etc.) in the spacecraft system as rigid and connected to the hub in parallel, significant computational efficiency is achieved through the unique form of the system mass matrix under these assumptions. The speed reduction is achieved by analytically backsolving the component couplings into the hub dynamics. As a result, rather than inverting the entire system mass matrix that scales with the cube of the number of states, instead only two 3×3 matrix inversions are required [21]. This method drastically reduces the computational overhead to simulate complex spacecraft systems [23].

In prior work, the backsubstitution method was used to develop force- and torque-based models of rigid-body or point-mass components that actuate in specific manners, such as single-hinged solar panels [24], spinning reaction wheels [25], control moment gyroscopes [26], multi-panel solar arrays with repeated hinge axes, and linear and spherical fuel mass particles [24]. Previous work by Carneiro et al. developed the capability to simulate chains of sequentially rotating or translating rigid bodies attached to the rigid spacecraft hub [27–29]. The developed formulations enable the simulation of telescoping and rotatable robotic arms and other chained structures. However, the nature of the backsubstitution method does not allow branching, open, or closed chains of spacecraft components. Branching and closed chains are impossible to simulate using the backsubstitution method due to the cross-coupling terms between components present in the system mass matrix. Similarly, open chains cannot be simulated simply by stacking components whose dynamics have already been formulated into the backsubstitution method. Instead, if the equations of motion for the entire open chain are developed using the backsubstitution formulation, the component configuration can be simulated. This approach captures the cross-coupling terms between subcomponents in the open chain. The performance and modularity benefits of the backsubstitution method come at the cost of these unallowable spacecraft configurations. However, a large range of spacecraft configurations can be simulated given the required assumptions.

This paper builds on previous multibody dynamics work using the backsubstitution method and expands its capabilities by developing a generalized, reconfigurable, and scalable method of describing prescribed motion spacecraft dynamics. An immediate benefit is that this solution enables more general spacecraft configurations to be modeled that can include branching and both open and closed chains through prescribed or servoed component motion models. Specifically, prescribed motion refers to spacecraft components whose actuation dynamics are one-way coupled with the other spacecraft components, meaning that their motion impacts the dynamics of the spacecraft system but not vice versa. Precise body-relative pointing of these components can be achieved using spacecraft servo subsystems such as stepper motors. Moreover, it is not necessary to completely derive the equations of motion of such components if their motion is instead prescribed through a commanded reference trajectory. As a result, some degrees of freedom of the system equations of motion may be eliminated for these prescribed components [30]. This appropriately reduces the computational overhead for complex spacecraft simulations. Several prescribed components are an integral part of NASA's Cassini spacecraft, including the articulated main engine, one-degree-of-freedom (1-DOF) probe relay antenna, and high-precision 2-DOF scan platform [30]. Other common examples of prescribed spacecraft elements include robotic systems, actuated motor platforms, gimbal thrusters, and servoed sensors.

Previous work in multibody prescribed motion dynamics has investigated a wide variety of applications. The motion of the Canadarm is one example of prescribed motion, where either the robotic arm can be commanded to follow preprogrammed prescribed trajectories, or its links can be directed to move through individual prescribed angles [30,31]. Ardakani and Bridges studied the dynamic coupling between a rigid vehicle following prescribed planar motion containing fluid and the fluid motion using Lagrangian mechanics [32]. Gerrits and Veldman studied the same problem using Newtonian and Eulerian mechanics [33,34]. Jain and Rodriguez develop a recursive algorithm to model the dynamics of a serial chain of hinges undergoing optional prescribed motion [30]. The formulated dynamics algorithm is applied to NASA's Cassini spacecraft, where it is used to model the articulated components aboard the spacecraft. The formulation is used in real-time aboard Cassini as part of its flexible multibody dynamics simulation software package.

In this study, a spacecraft consisting of a rigid hub and N prescribed motion rigid subcomponents is considered for the dynamics formulation. The 6-DOF of each subcomponent are assumed to be prescribed relative to the spacecraft hub. For example, consider a spacecraft that is deploying an N-element solar panel with servo motors. The motion of the panel is prescribed by the motors, and hence there are no free degrees of freedom associated with this motion. To simulate any type of spacecraft component actuation generally, the component can be considered as a collection of N connected rigid subcomponents. Each subcomponent can be considered a prescribed motion body whose motion contributes to the overall three-dimensional motion of the actuated spacecraft component. The prescribed motion dynamics in this work are derived with the assumption that the hub-relative states of each subcomponent can be identified relative to a reference frame that is fixed to the spacecraft hub. Each subcomponent may be commanded to translate and rotate generally in three-dimensional space with respect to the spacecraft hub, enabling the simulation of any type of actuated spacecraft component motion. Thus, this paper develops a general spacecraft dynamics model describing how N-element rigid bodies can undergo 6-DOF prescribed hub-relative motion. Although the derived dynamics do not capture the coupling effect of other system bodies on the prescribed component motion, this approach is reasonable for modeling the bulk motion of actuated spacecraft components that are tightly controlled and less susceptible to flexing behavior. Additionally, this approach assumes no sensing or actuation problems occur when commanding or actuating these prescribed components. If their true motion deviates from the assumed prescribed trajectory, this approach is not effective.

To meet the needs of these evolving spacecraft concepts, significant software advancements are required to expand the existing simulation space and capture these complex spacecraft systems. The dynamics of multibody systems are challenging to verify and implement in software in a generalized, modular manner due to the wide range of complex spacecraft configurations or simulation environmental factors that are desired. Open-source multibody dynamics software packages such as Project CHRONO,[§] Moby,[¶] Bullet,[**] POEMS [35], and the Rigid Body Dynamics Library[††] all excel at simulating very large multibody spacecraft structures; however, the ability to incorporate relevant simulation environmental

[§]Data available online at http://projectchrono.org.

[¶]Data available online at http://physsim.sourceforge.net/index.html.

[**]Data available online at http://bulletphysics.org/wordpress/.

[††]Data available online at https://rbdl.github.io/.

factors or mission-specific flight software algorithms is not readily available with these packages. Moreover, while commercial software packages such as COMSOL,[‡‡] Adams,[§§] MathWork's Simscape Multibody,[¶] and the symbolic software MotionGenesis[***] are proficient at computing and providing the equations of motion for specific multibody dynamic systems, but they are unable to provide generalized equations of motion that are widely applicable to multiple different types of complex dynamic systems. Spacecraft-specific software packages such as the Jet Propulsion Laboratory's Dynamics Algorithms for Real-Time Simulation (DARTS),[†††] STK SOLIS,[‡‡‡] NASA's open-source package 42,[§§§] and the Basilisk astrodynamics simulation framework[¶¶¶] are advantageous choices for addressing specific spacecraft-centric simulation challenges such as the implementation of environmental disturbances or flight software algorithms into the simulation. For these reasons, Basilisk is the simulation software architecture chosen in this work to implement and verify the derived multibody prescribed motion dynamics. This open-source software framework leverages the backsubstitution method and has been widely used for mission analysis. While Basilisk offers similar advantages to other simulation tools, its unique combination of capabilities sets it apart from all others [21,22]. Its highly modular architecture, combined with its dynamic generality, computational efficiency, scalability, and intuitive Python scripting interface, makes it an ideal software choice for this work.

The organization of this paper is as follows: First, the problem statement for the spacecraft system containing prescribed motion subcomponents is given, and the required parameters and reference frame definitions for the dynamics derivation are established (Sec. II). Next, Sec. III provides an overview of the backsubstitution method that serves as the foundation for this work. Section IV derives the spacecraft hub equations of motion using Newtonian and Eulerian mechanics, although it should be noted that an abundance of other methods could be chosen to develop the spacecraft dynamics [36,37]. The final equations are manipulated into the form of the backsubstitution method to facilitate a modular software implementation. Section V provides a prescribed solar array deployment simulation scenario, demonstrating the scalability of the dynamics formulation, and the concluding remarks are offered in Sec. VI. The kinematic profiler modules developed to prescribe the subcomponent motion are discussed, and the complete mathematics are given in Appendix A. Finally, the verification of the derived dynamics is given in Appendix B.

II. Problem Statement

This work develops the equations of motion for a multibody spacecraft system consisting of a rigid hub and N kinematically prescribed rigid subcomponents with complete generality. Provided that each body is rigid in the derivation, no other assumptions are made regarding the mass properties of each body. All reference frames are located and oriented generally with respect to each other. Accordingly, these choices enable a wide range of spacecraft configurations to be readily integrated into a software simulation without the need for future rederivation of the equations of motion. The spacecraft system problem statement for this derivation is illustrated in Fig. 1. Although only one prescribed subcomponent (green) is shown, the formulation assumes N subcomponents are contained in the spacecraft system.

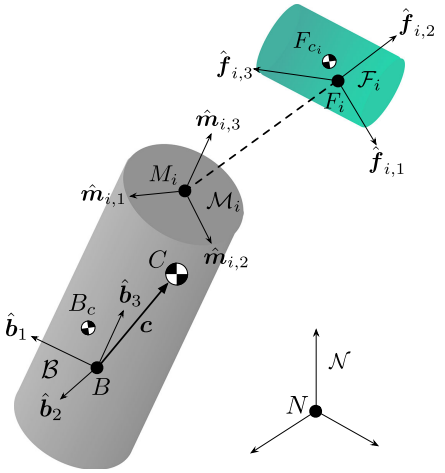

Fig. 1 Spacecraft system problem statement.

Four reference frames are used to define the spacecraft system given by Fig. 1. First, the dynamics are developed with respect to an inertial reference frame indicated by $\mathcal{N}:\{N, \hat{\boldsymbol{n}}_1, \hat{\boldsymbol{n}}_2, \hat{\boldsymbol{n}}_3\}$. The hub body frame $\mathcal{B}:\{B, \hat{\boldsymbol{b}}_1, \hat{\boldsymbol{b}}_2, \hat{\boldsymbol{b}}_3\}$ describes the motion of the rigid spacecraft hub of mass m_{hub}. The origin of this frame is located at the hub-fixed point B. The point B_c defines the center of mass of the hub, which is also body-fixed as a result of the rigid-body assumption, i.e., $\boldsymbol{r}'_{B_c/B} = \boldsymbol{0}$. The right $'$ superscript indicates a hub $\mathcal{B}$ frame-relative time derivative. Although points B and B_c are often assumed to coincide for a simpler equations of motion formulation, they are kept distinct in order to improve the ease of technical exchanges between spacecraft mission teams. For example, a structure frame is often defined by the structural engineering team that is used to define the location of all the spacecraft components relative to a single fixed location on the spacecraft hub.

The mass of the subcomponents is given by m_{P_i}, and their body frames are designated by $\mathcal{F}_i:\{F_i, \hat{\boldsymbol{f}}_{i,1}, \hat{\boldsymbol{f}}_{i,2}, \hat{\boldsymbol{f}}_{i,3}\}$. The origin points F_i of each frame and the center of mass points F_{c_i} of each subcomponent are fixed to the subcomponents, i.e., $({}^{\mathcal{F}_i}\mathrm{d}/\mathrm{d}t)\boldsymbol{r}_{F_{c_i}/F_i} = \boldsymbol{0}$. These frames describe the motion of each subcomponent relative to a hub-fixed mount interface indicated by the frame $\mathcal{M}_i:\{M_i, \hat{\boldsymbol{m}}_{i,1}, \hat{\boldsymbol{m}}_{i,2}, \hat{\boldsymbol{m}}_{i,3}\}$. Introduced as a matter of kinematic convenience, the locations and orientations of the mount frames are fixed with respect to the hub, i.e., $\boldsymbol{r}'_{M_i/B} = \boldsymbol{\omega}_{\mathcal{M}_i/\mathcal{B}} = \boldsymbol{0}$. Further, the vector $\boldsymbol{c}$ describes the system center of mass location relative to point B , where C denotes the system center of mass point. Note that for a completely general equations of motion formulation, the points $B, B_c, F_i, F_{c_i}, M_i$, and C are assumed not to be necessarily coincident.

The translational and rotational states required to explicitly profile the hub-relative prescribed subcomponent 6-DOF motion are given by $\boldsymbol{r}_{F_i/M_i}, \boldsymbol{r}'_{F_i/M_i}, \boldsymbol{r}''_{F_i/M_i}, \boldsymbol{\sigma}_{\mathcal{F}_i/\mathcal{M}_i}, \boldsymbol{\omega}_{\mathcal{F}_i/\mathcal{M}_i}$, and $\boldsymbol{\omega}'_{\mathcal{F}_i/\mathcal{M}_i}$. Although they are implicitly contained in the equations of motion derived in Sec. IV, these terms are explicitly exposed throughout the intermediate steps of the derivation process. Finally, note that modified Rodriguez parameter attitude coordinates [36] are selected to express the relative orientations between reference frames, facilitating integration with the Basilisk software. However, note that alternative representations, such as quaternions or direction cosine matrices, can also be used.

III. Backsubstitution Method

For multibody spacecraft systems, the spacecraft dynamics are often derived in the form $[M]\dot{\boldsymbol{X}} = \boldsymbol{f}(\boldsymbol{X}, t)$, where $[M]$ is the system mass matrix, $\boldsymbol{X}$ is the system state vector, $\dot{\boldsymbol{X}}$ is the time derivative of the state vector, and $\boldsymbol{f}(\boldsymbol{X}, t)$ is a function of the state vector and time. It is clear that the size of the system mass matrix grows significantly as the number of rigid bodies in the spacecraft system increases,

[‡‡]Data available online at https://www.comsol.com/multibody-dynamics-module.

[§§]Data available online at http://www.mscsoftware.com/product/adams.

[¶]Data available online at https://www.mathworks.com/products/simmechanics.html.

[***]Data available online at https://www.motiongenesis.com/.

[†††]Data available online at https://dartslab.jpl.nasa.gov/DARTS/index.php.

[‡‡‡]Data available online at https://help.agi.com/stk/Subsystems/solis/solis.htm.

[§§§]Data available online at https://software.nasa.gov/software/GSC-16720-1.

[¶¶¶]Data available online at https://avslab.github.io/basilisk.

thus making inversion of the mass matrix to obtain the desired form for numerical integration, $\dot{\boldsymbol{X}} = \boldsymbol{g}(\boldsymbol{X}, t)$, more computationally expensive. Moreover, the software implementation, organization, and testing framework of the resulting equations of motion become particularly difficult when considering large, complex spacecraft structures.

The backsubstitution method [21–23] was recently developed to address these concerns, where a modular dynamics formulation enables the rapid creation, execution, and testing of complex multibody spacecraft simulations. Fundamental to the backsubstitution method is the requirement of a hub-centric spacecraft configuration, where articulating components or effectors are attached in parallel to the spacecraft hub. Components whose dynamics have already been formulated into the backsubstitution method cannot be chained together under this assumption. Instead, the equations of motion for the entire chained structure must be formulated as a single effector into the backsubstitution method in order to simulate these configurations. The computational speed and modularity of the backsubstitution method are achieved through exploiting the unique structure of the system mass matrix resulting from this requirement.

Allard et al. present a generalized system mass matrix form for N dual-hinged panels connected to a central rigid hub to illustrate the coupling between the system components under the requirements of the backsubstitution method [21]. A simplified version for M single-hinged chained panels connected in parallel is presented in Eq. (2) to illustrate this concept, where $\ddot{\boldsymbol{r}}_{B/N}$ is the hub inertial translational acceleration and $\dot{\boldsymbol{\omega}}_{\mathcal{B}/\mathcal{N}}$ is the hub inertial angular acceleration. The relative angular acceleration of each panel i about its 1-DOF hinge axis is denoted $\ddot{\theta}_i$.

$$\begin{bmatrix} [\cdot]_{3\times3} & [\cdot]_{3\times3} & [\cdot]_{3\times1} & [\cdot]_{3\times1} & \cdots & [\cdot]_{3\times1} \\ [\cdot]_{3\times3} & [\cdot]_{3\times3} & [\cdot]_{3\times1} & [\cdot]_{3\times1} & \cdots & [\cdot]_{3\times1} \\ [\cdot]_{1\times3} & [\cdot]_{1\times3} & [\cdot]_{1\times1} & [0]_{1\times1} & \cdots & [0]_{1\times1} \\ [\cdot]_{1\times3} & [\cdot]_{1\times3} & [0]_{1\times1} & [\cdot]_{1\times1} & \cdots & [0]_{1\times1} \\ \cdots & \cdots & \cdots & \cdots & \cdots & \cdots \\ [\cdot]_{1\times3} & [\cdot]_{1\times3} & [0]_{1\times1} & [0]_{1\times1} & \cdots & [\cdot]_{1\times1} \end{bmatrix} \begin{bmatrix} \ddot{\boldsymbol{r}}_{B/N} \\ \dot{\boldsymbol{\omega}}_{\mathcal{B}/\mathcal{N}} \\ \ddot{\theta}_1 \\ \ddot{\theta}_2 \\ \cdots \\ \ddot{\theta}_M \end{bmatrix} = \begin{bmatrix} [\cdot]_{3\times1} \\ [\cdot]_{3\times1} \\ [\cdot]_{1\times1} \\ [\cdot]_{1\times1} \\ \cdots \\ [\cdot]_{1\times1} \end{bmatrix} \tag{1}$$

Viewing Eq. (2), it is clear that the hub second-order state variables are coupled with all of the subcomponent second-order states and vice versa; however, the second-order states of the subcomponents are not coupled together. This results in a block-diagonal for all effector-on-effector associations. Similarly, for spacecraft with multibody effectors derived in the form of the backsubstitution method, there are no cross-couplings between effectors; however, there are coupling terms within each effector. This results in a near block-diagonal form for the effector-on-effector mass matrix associations. As a result of this matrix structure, instead of inverting the entire system mass matrix, only two 3×3 matrix inversions are required. This becomes clear when expressing the subcomponent equations above in the matrix form

$$[\ddot{\boldsymbol{\theta}}] = [\boldsymbol{A}_\theta]\ddot{\boldsymbol{r}}_{B/N} + [\boldsymbol{B}_\theta]\dot{\boldsymbol{\omega}}_{\mathcal{B}/\mathcal{N}} + [\boldsymbol{C}_\theta] \tag{2}$$

where the $[\boldsymbol{A}_\theta]$ and $[\boldsymbol{B}_\theta]$ matrices contain the coupling terms between the subcomponents and the hub and the $[\boldsymbol{C}_\theta]$ matrix contains the remaining terms. It is in this form that the subcomponent equation can be "backsubstituted" into the hub equations of motion, yielding the condensed result

$$\begin{bmatrix} [A] & [B] \\ [C] & [D] \end{bmatrix} \begin{bmatrix} \ddot{\boldsymbol{r}}_{B/N} \\ \dot{\boldsymbol{\omega}}_{\mathcal{B}/\mathcal{N}} \end{bmatrix} = \begin{bmatrix} \boldsymbol{v}_{\text{trans}} \\ \boldsymbol{v}_{\text{rot}} \end{bmatrix} \tag{3}$$

Modularizing the hub equations of motion in this manner enables extensive scalability of spacecraft simulations, where the effector contributions can be iteratively aggregated in parallel. The hub accelerations can be directly solved using Eq. (3), where only two 3×3 matrix inversions are required [21]:

$$\dot{\boldsymbol{\omega}}_{\mathcal{B}/\mathcal{N}} = \left([D] - [C][A]^{-1}[B]\right)^{-1}\left(\boldsymbol{v}_{\text{rot}} - [C][A]^{-1}\boldsymbol{v}_{\text{trans}}\right) \tag{4}$$

$$\ddot{\boldsymbol{r}}_{B/N} = [A]^{-1}\left(\boldsymbol{v}_{\text{trans}} - [B]\dot{\boldsymbol{\omega}}_{\mathcal{B}/\mathcal{N}}\right) \tag{5}$$

Finally, the remaining subcomponent accelerations can be solved by substituting the hub accelerations back into Eq. (2). The system can be numerically integrated using these results.

Note that for the spacecraft system in this work, there are $6(N + 1)$ total system degrees of freedom, where $6N$ are known (prescribed), and the remaining six are the hub translational and rotational degrees of freedom. Therefore, only six differential equations for the six hub degrees of freedom need to be derived, and Eq. (2) is not needed.

IV. Derivation of Hub Equations of Motion with Prescribed Subcomponent Kinematics

This section derives the equations of motion for the spacecraft system of interest in the form of the backsubstitution method, requiring the rigid hub dynamics to be developed rather than the spacecraft system center-of-mass dynamics. Using Newtonian and Eulerian mechanics, the spacecraft hub translational and rotational equations of motion are first developed with complete generality. The resulting equations are compact and frame-independent. The hub equations of motion are finally manipulated into the form of the backsubstitution method contributions given by Eq. (3), enabling a modular software implementation.

A. Translational Equations of Motion

The spacecraft hub translational equations of motion define the first three system degrees of freedom. These equations are derived starting from Newton's Second Law for the spacecraft center of mass [36]:

$$m_{\text{sc}}\ddot{\boldsymbol{r}}_{C/N} = m_{\text{sc}}\ddot{\boldsymbol{c}} + m_{\text{sc}}\ddot{\boldsymbol{r}}_{B/N} = \boldsymbol{F}_{\text{ext}} \tag{6}$$

where m_{sc} is the total mass of the spacecraft system, $m_{\text{sc}} = m_{\text{hub}} + \sum_{i=1}^{N} m_{P_i}$, and $\boldsymbol{F}_{\text{ext}}$ is the sum of all external forces acting on the system. Note that because the hub equations of motion are of interest for this formulation, the acceleration of the hub frame origin point B must be defined. First, the transport theorem [36] is used to relate the hub-relative derivative of the center of mass vector to its inertial time derivative:

$$\dot{\boldsymbol{c}} = \boldsymbol{c}' + \boldsymbol{\omega}_{\mathcal{B}/\mathcal{N}} \times \boldsymbol{c} \tag{7}$$

$$\ddot{\boldsymbol{c}} = \boldsymbol{c}'' + 2\boldsymbol{\omega}_{\mathcal{B}/\mathcal{N}} \times \boldsymbol{c}' + \dot{\boldsymbol{\omega}}_{\mathcal{B}/\mathcal{N}} \times \boldsymbol{c} + \boldsymbol{\omega}_{\mathcal{B}/\mathcal{N}} \times \boldsymbol{\omega}_{\mathcal{B}/\mathcal{N}} \times \boldsymbol{c} \tag{8}$$

The system center of mass vector is defined using the mass contributions from the hub and N prescribed subcomponents:

$$\boldsymbol{c} = \frac{m_{\text{hub}}\boldsymbol{r}_{B_c/B} + \sum_{i=1}^{N} m_{P_i}\boldsymbol{r}_{F_{c_i}/B}}{m_{\text{sc}}} \tag{9}$$

The hub-relative velocity of the center of mass vector is

$$\boldsymbol{c}' = \frac{\sum_{i=1}^{N} m_{P_i}\boldsymbol{r}'_{F_{c_i}/B}}{m_{\text{sc}}} \tag{10}$$

where using the transport theorem yields

$$\boldsymbol{r}'_{F_{c_i}/B} = \boldsymbol{r}'_{F_{c_i}/F_i} + \boldsymbol{r}'_{F_i/M_i} + \boldsymbol{r}'_{M_i/B} = \boldsymbol{\omega}_{\mathcal{F}_i/\mathcal{M}} \times \boldsymbol{r}_{F_{c_i}/F_i} + \boldsymbol{r}'_{F_i/M_i} \tag{11}$$

Similarly, the hub-relative acceleration of the center of mass vector is

$$\boldsymbol{c}'' = \frac{\sum_{i=1}^{N} m_{P_i} \boldsymbol{r}''_{F_{c_i}/B}}{m_{\text{sc}}} \tag{12}$$

where

$$\begin{aligned}\boldsymbol{r}''_{F_{c_i}/B} &= \boldsymbol{\omega}'_{\mathcal{F}_i/\mathcal{M}} \times \boldsymbol{r}_{F_{c_i}/F_i} + \boldsymbol{\omega}_{\mathcal{F}_i/\mathcal{M}} \times \boldsymbol{r}'_{F_{c_i}/F_i} + \boldsymbol{r}''_{F_i/M_i} \\ &= \left([\tilde{\boldsymbol{\omega}}'_{\mathcal{F}_i/\mathcal{M}}] + [\tilde{\boldsymbol{\omega}}_{\mathcal{F}_i/\mathcal{M}}]^2\right)\boldsymbol{r}_{F_{c_i}/F_i} + \boldsymbol{r}''_{F_i/M_i}\end{aligned} \tag{13}$$

Equation (13) introduces the matrix cross-product operator, where for an arbitrary vector $\boldsymbol{v} = [v_1, v_2, v_3]^T$, the corresponding matrix cross-product operator is given by $[\tilde{\boldsymbol{v}}]$

$$[\tilde{\boldsymbol{v}}] = \begin{bmatrix} 0 & -v_3 & v_2 \\ v_3 & 0 & -v_1 \\ -v_2 & v_1 & 0 \end{bmatrix} \tag{14}$$

Substituting Eqs. (8) and (12) into Eq. (6) and arranging the terms in the form of the backsubstitution method yields the system translational equations of motion:

$$\begin{aligned}m_{\text{sc}}\ddot{\boldsymbol{r}}_{B/N} + m_{\text{sc}}[\dot{\tilde{\boldsymbol{\omega}}}_{\mathcal{B}/\mathcal{N}}]\boldsymbol{c} = \boldsymbol{F}_{\text{ext}} - 2m_{\text{sc}}[\tilde{\boldsymbol{\omega}}_{\mathcal{B}/\mathcal{N}}]\boldsymbol{c}' - m_{\text{sc}}[\tilde{\boldsymbol{\omega}}_{\mathcal{B}/\mathcal{N}}]^2\boldsymbol{c} \\ - \sum_{i=1}^{N} m_{P_i}\boldsymbol{r}''_{F_{c_i}/B}\end{aligned} \tag{15}$$

B. Rotational Equations of Motion

The spacecraft hub rotational equations of motion describe the three remaining hub degrees of freedom. The equations are developed by separating the kinematic and kinetic differential equations. This enables convenient use of the angular velocity vector $\boldsymbol{\omega}_{\mathcal{B}/\mathcal{N}}$ in the kinetic rotational equations of motion while not limiting the choice of attitude coordinates used to describe the hub kinematic orientation. The derivation begins by applying Euler's equation to the case where the spacecraft angular momentum is expressed about a hub-fixed point not coincident with the system center of mass [36]:

$$\dot{\boldsymbol{H}}_{\text{sc},B} = \boldsymbol{L}_B + m_{\text{sc}}\ddot{\boldsymbol{r}}_{B/N} \times \boldsymbol{c} \tag{16}$$

where $\boldsymbol{H}_{\text{sc},B}$ is the inertial angular momentum of the spacecraft system about point B and $\boldsymbol{L}_B$ is the total external torque acting on the system about point B. First, the system's angular momentum about point B is

$$\begin{aligned}\boldsymbol{H}_{\text{sc},B} &= \boldsymbol{H}_{\text{hub},B} + \sum_{i=1}^{N} \boldsymbol{H}_{P_i,B} \\ &= [I_{\text{hub},B}]\boldsymbol{\omega}_{\mathcal{B}/\mathcal{N}} + \sum_{i=1}^{N}\left(\boldsymbol{H}_{P_i,F_{c_i}} + m_{P_i}\boldsymbol{r}_{F_{c_i}/B} \times \dot{\boldsymbol{r}}_{F_{c_i}/B}\right) \\ &= [I_{\text{hub},B}]\boldsymbol{\omega}_{\mathcal{B}/\mathcal{N}} + \sum_{i=1}^{N}\Big([I_{P_i,B}]\boldsymbol{\omega}_{\mathcal{B}/\mathcal{N}} + [I_{P_i,F_{c_i}}]\boldsymbol{\omega}_{\mathcal{F}_i/\mathcal{M}_i} \\ &\quad + m_{P_i}[\tilde{\boldsymbol{r}}_{F_{c_i}/B}]\boldsymbol{r}'_{F_{c_i}/B}\Big)\end{aligned} \tag{17}$$

where $[I_{\text{hub},B}]$ is the hub inertia tensor about point B, $[I_{P_i,F_{c_i}}]$ are the subcomponent inertia tensors about their centers of mass, and $[I_{P_i,B}]$ are the subcomponent inertia tensors about point B. Combining all inertia tensors about point B yields the total spacecraft inertia about point B:

$$[I_{\text{sc},B}] = [I_{\text{hub},B}] + \sum_{i=1}^{N}[I_{P_i,B}] \tag{18}$$

Equation (17) becomes

$$\boldsymbol{H}_{\text{sc},B} = [I_{\text{sc},B}]\boldsymbol{\omega}_{\mathcal{B}/\mathcal{N}} + \sum_{i=1}^{N}\left([I_{P_i,F_{c_i}}]\boldsymbol{\omega}_{\mathcal{F}_i/\mathcal{M}_i} + m_{P_i}[\tilde{\boldsymbol{r}}_{F_{c_i}/B}]\boldsymbol{r}'_{F_{c_i}/B}\right) \tag{19}$$

Next, the inertial time derivative of the total spacecraft angular momentum is expressed using the transport theorem as

$$\begin{aligned}\dot{\boldsymbol{H}}_{\text{sc},B} &= \boldsymbol{H}'_{\text{sc},B} + \boldsymbol{\omega}_{\mathcal{B}/\mathcal{N}} \times \boldsymbol{H}_{\text{sc},B} \\ &= \boldsymbol{H}'_{\text{sc},B} + [\tilde{\boldsymbol{\omega}}_{\mathcal{B}/\mathcal{N}}][I_{\text{sc},B}]\boldsymbol{\omega}_{\mathcal{B}/\mathcal{N}} \\ &\quad + \sum_{i=1}^{N}\left([\tilde{\boldsymbol{\omega}}_{\mathcal{B}/\mathcal{N}}][I_{P_i,F_{c_i}}]\boldsymbol{\omega}_{\mathcal{F}_i/\mathcal{M}_i} + m_{P_i}[\tilde{\boldsymbol{\omega}}_{\mathcal{B}/\mathcal{N}}][\tilde{\boldsymbol{r}}_{F_{c_i}/B}]\boldsymbol{r}'_{F_{c_i}/B}\right)\end{aligned} \tag{20}$$

The $\mathcal{B}$ frame time derivative of the system angular momentum is

$$\begin{aligned}\boldsymbol{H}'_{\text{sc},B} &= [I'_{\text{sc},B}]\boldsymbol{\omega}_{\mathcal{B}/\mathcal{N}} + [I_{\text{sc},B}]\dot{\boldsymbol{\omega}}_{\mathcal{B}/\mathcal{N}} \\ &\quad + \sum_{i=1}^{N}\left([I'_{P_i,F_{c_i}}]\boldsymbol{\omega}_{\mathcal{F}_i/\mathcal{M}_i} + [I_{P_i,F_{c_i}}]\boldsymbol{\omega}'_{\mathcal{F}_i/\mathcal{M}_i} + m_{P_i}[\tilde{\boldsymbol{r}}_{F_{c_i}/B}]\boldsymbol{r}''_{F_{c_i}/B}\right)\end{aligned} \tag{21}$$

Using the rigid-body assumption for the hub and the parallel axis theorem to express the subcomponent inertias about point B yields the $\mathcal{B}$ frame derivative of the spacecraft inertia tensor:

$$\begin{aligned}[I'_{\text{sc},B}] &= \sum_{i=1}^{N}[I'_{P_i,B}] \\ &= \sum_{i=1}^{N}\left([I'_{P_i,F_{c_i}}] + m_{P_i}\left([\tilde{\boldsymbol{r}}'_{F_{c_i}/B}][\tilde{\boldsymbol{r}}_{F_{c_i}/B}]^T + [\tilde{\boldsymbol{r}}_{F_{c_i}/B}][\tilde{\boldsymbol{r}}'_{F_{c_i}/B}]^T\right)\right)\end{aligned} \tag{22}$$

The inertia transport theorem [38] is used to express the subcomponent inertias about their centers of mass:

$$[I'_{P_i,F_{c_i}}] = [\tilde{\boldsymbol{\omega}}_{\mathcal{F}_i/\mathcal{M}_i}][I_{P_i,F_{c_i}}] - [I_{P_i,F_{c_i}}][\tilde{\boldsymbol{\omega}}_{\mathcal{F}_i/\mathcal{M}_i}] \tag{23}$$

Equation (22) becomes

$$\begin{aligned}[I'_{\text{sc},B}] = \sum_{i=1}^{N}\Big([\tilde{\boldsymbol{\omega}}_{\mathcal{F}_i/\mathcal{M}_i}][I_{P_i,F_{c_i}}] - [I_{P_i,F_{c_i}}][\tilde{\boldsymbol{\omega}}_{\mathcal{F}_i/\mathcal{M}_i}] \\ + m_{P_i}\left([\tilde{\boldsymbol{r}}'_{F_{c_i}/B}][\tilde{\boldsymbol{r}}_{F_{c_i}/B}]^T + [\tilde{\boldsymbol{r}}_{F_{c_i}/B}][\tilde{\boldsymbol{r}}'_{F_{c_i}/B}]^T\right)\Big)\end{aligned} \tag{24}$$

Combining these results and arranging the terms in the form of the backsubstitution method yields the system rotational equations of motion:

$$\begin{aligned}m_{\text{sc}}[\tilde{\boldsymbol{c}}]\ddot{\boldsymbol{r}}_{B/N} + [I_{\text{sc},B}]\dot{\boldsymbol{\omega}}_{\mathcal{B}/\mathcal{N}} &= \boldsymbol{L}_B - \left([I'_{\text{sc},B}] + [\tilde{\boldsymbol{\omega}}_{\mathcal{B}/\mathcal{N}}][I_{\text{sc},B}]\right)\boldsymbol{\omega}_{\mathcal{B}/\mathcal{N}} \\ &\quad - \sum_{i=1}^{N}\Big(m_{P_i}[\tilde{\boldsymbol{r}}_{F_{c_i}/B}]\boldsymbol{r}''_{F_{c_i}/B} - [I_{P_i,F_{c_i}}]\boldsymbol{\omega}'_{\mathcal{F}_i/\mathcal{M}_i} \\ &\quad - m_{P_i}[\tilde{\boldsymbol{\omega}}_{\mathcal{B}/\mathcal{N}}][\tilde{\boldsymbol{r}}_{F_{c_i}/B}]\boldsymbol{r}'_{F_{c_i}/B} - \left([I'_{P_i,F_{c_i}}] + [\tilde{\boldsymbol{\omega}}_{\mathcal{B}/\mathcal{N}}][I_{P_i,F_{c_i}}]\right)\boldsymbol{\omega}_{\mathcal{F}_i/\mathcal{M}_i}\Big)\end{aligned} \tag{25}$$

C. Backsubstitution Formulation

Recall that the equations of motion given in Eqs. (15) and (25) fully define the hub translational and rotational degrees of freedom. Accordingly, no additional equations of motion need to be developed to resolve the remaining $6N$ prescribed subcomponent degrees of freedom. The developed equations of motion are therefore already written in the final form of the backsubstitution method and yield a modular simulation capability. The $[A]$, $[B]$, $[C]$, and $[D]$ matrices seen in Eq. (3) are obtained by collecting all left-hand terms from the equations

$$[A] = m_{\text{sc}}[I_{3\times 3}] \tag{26}$$

$$[B] = -m_{\text{sc}}[\tilde{\boldsymbol{c}}] \tag{27}$$

$$[C] = m_{\text{sc}}[\tilde{\boldsymbol{c}}] \tag{28}$$

$$[D] = [I_{\text{sc},B}] \tag{29}$$

The $\boldsymbol{v}_{\text{trans}}$ and $\boldsymbol{v}_{\text{rot}}$ vector components contain the remaining right-hand side terms:

$$\boldsymbol{v}_{\text{trans}} = \boldsymbol{F}_{\text{ext}} - 2m_{\text{sc}}[\tilde{\boldsymbol{\omega}}_{\mathcal{B}/\mathcal{N}}]\boldsymbol{c}' - m_{\text{sc}}[\tilde{\boldsymbol{\omega}}_{\mathcal{B}/\mathcal{N}}]^2\boldsymbol{c} - \sum_{i=1}^{N} m_{P_i}\boldsymbol{r}''_{F_{c_i}/B} \tag{30}$$

$$\begin{aligned}\boldsymbol{v}_{\text{rot}} = {} & \boldsymbol{L}_B - \Big([I'_{\text{sc},B}] + [\tilde{\boldsymbol{\omega}}_{\mathcal{B}/\mathcal{N}}][I_{\text{sc},B}]\Big)\boldsymbol{\omega}_{\mathcal{B}/\mathcal{N}} \\ & - \sum_{i=1}^{N}\Big(m_{P_i}[\tilde{\boldsymbol{r}}_{F_{c_i}/B}]\boldsymbol{r}''_{F_{c_i}/B} - [I_{P_i,F_{c_i}}]\boldsymbol{\omega}'_{\mathcal{F}_i/\mathcal{M}_i} \\ & - m_{P_i}[\tilde{\boldsymbol{\omega}}_{\mathcal{B}/\mathcal{N}}][\tilde{\boldsymbol{r}}_{F_{c_i}/B}]\boldsymbol{r}'_{F_{c_i}/B} - \Big([I'_{P_i,F_{c_i}}] + [\tilde{\boldsymbol{\omega}}_{\mathcal{B}/\mathcal{N}}][I_{P_i,F_{c_i}}]\Big)\boldsymbol{\omega}_{\mathcal{F}_i/\mathcal{M}_i}\Big)\end{aligned} \tag{31}$$

The backsubstitution contributions above highlight the one-way coupling present between the prescribed subcomponents and the spacecraft hub. Recall that the $[A]$, $[B]$, $[C]$, and $[D]$ matrices contain all terms coupled with the hub accelerations. Equations (26–29) contain only mass properties of the spacecraft system and do not include mass and inertia contributions associated with the subcomponent accelerations, indicating that the hub accelerations do not impact the subcomponent dynamics. Further, note that the subcomponent prescribed states appear in both Eqs. (30) and (31). The subcomponent translational and rotational accelerations appear implicitly and explicitly in these equations, respectively, demonstrating that the hub accelerations are indeed impacted by the subcomponent accelerations.

V. Numerical Simulation

The prescribed motion dynamics derived in this work are valid for any number of subcomponents whose motion can be prescribed relative to a rigid spacecraft hub. To illustrate the complex simulation capability and scalability that is enabled with this body of work, this section presents a multibody rotational solar array deployment scenario inspired by the NASA Lucy mission ultra-flex lanyard-driven solar array deployment. The required spacecraft model, frame definitions, and parameters required to simulate the array deployment scenario are first presented, followed by a brief discussion of the kinematic profiler modules developed to prescribe the subcomponent hub-relative motion during the deployment. The complete mathematics used to profile the subcomponent motion is given in Appendix A. The simulation results are lastly presented, and the hub response to the array deployment is evaluated. The complete source code developed in this work is available in the open-source Basilisk[****] repository.

****Data available online at https://github.com/AVSLab/basilisk.

A. Simulation Setup

The relevant simulation parameters chosen for this scenario are presented in Table 1. The spacecraft system consists of a central rigid hub with two symmetrically attached circular solar arrays. Each solar array is modeled as a collection of N rigid element subcomponents. The arrays are deployed individually rather than simultaneously to reflect a single mission design choice. The deployment scenario is seen in Fig. 2. The array element subcomponents are initially oriented in the stowed configuration shown in Fig. 2a, where they are stacked together into a wedge-like shape. Further, each array deploys in two stages. The first stage is the *initial deployment phase*, where the stacked elements rotate together from the stowed configuration away from the spacecraft hub into the initial deployment configuration. The initial array 1 deployment configuration is illustrated in Fig. 2b. The initial deployment configuration for array 2 is shown in Fig. 2d. The second stage is the *main deployment stage*, where the elements begin to unfurl to their deployed locations. The configuration with both arrays fully deployed is illustrated in Fig. 2e.

The spacecraft geometry and required frame definitions for the deployment scenario are illustrated in Fig. 3. Figure 3a illustrates the stowed frame orientations, and Fig. 3b presents both array initial deployment configurations for clarity. Both arrays are included in the latter figure for the purpose of compactness. The rigid hub body frame is denoted $\mathcal{B}:\{B, \hat{\boldsymbol{b}}_1, \hat{\boldsymbol{b}}_2, \hat{\boldsymbol{b}}_3\}$ and is located at the hub center of mass point B_c. The solar arrays are symmetrically mounted to the hub at the hub-fixed points M_1 and M_2. Solar array 1 is designated as the array mounted along the positive $\hat{\boldsymbol{b}}_1$ axis. Each individual array element's kinematic motion is profiled relative to a hub-fixed mount frame denoted as $\mathcal{M}_i:\{M_i, \hat{\boldsymbol{m}}_{i_1}, \hat{\boldsymbol{m}}_{i_2}, \hat{\boldsymbol{m}}_{i_3}\}$, where $i = 1{,}2$. The mount frames in the scenario have the same orientation as the spacecraft body frame, as seen in Fig. 3. Therefore, the angular velocity of each mount frame with respect to the hub frame $\boldsymbol{\omega}_{\mathcal{M}_i/\mathcal{B}}$ is fixed at zero for the deployment scenario. The body frame of each rigid element is denoted $\mathcal{F}_{ij}:\{F_{ij}, \hat{\boldsymbol{f}}_{ij_1}, \hat{\boldsymbol{f}}_{ij_2}, \hat{\boldsymbol{f}}_{ij_3}\}$, where $j = 1 \cdots N$ denotes the jth array element and $i = 1{,}2$ for each solar array. Accordingly, the translational and rotational motion of each array element is profiled using the array element body frames $\mathcal{F}_{ij}$ relative to their respective mount frame $\mathcal{M}_i$.

B. Kinematic Profiler Development for Prescribed Subcomponent Hub-Relative States

Recall that because the hub-relative states of the subcomponents are assumed to be explicitly known and prescribed at all instances in time, no equations of motion are needed for these spacecraft components. Therefore, in order to simulate the motion of these components and integrate their dynamics into the hub equations of motion, a time history of the subcomponent hub-relative translational and rotational states must be available during all phases of the spacecraft mission. To achieve this functionality, modular translational and rotational kinematic profiler modules are developed to specify the subcomponent states at each instant in time while simultaneously incorporating these states into the subcomponent terms on the right-hand side of Eq. (3).

Generally, it is clear that an unlimited number of profilers could be written to capture any conceivable type of subcomponent motion. Note that the subcomponent's hub-relative translational states can be profiled separately from its rotational states, although strict discretion must be used to ensure that the profiled motion is realistic such that no fundamental laws of physics are violated. In this work, two basic profiler modules are developed to prescribe the subcomponents' hub-relative motion for the solar array deployment scenario. The first module prescribes linear translational motion relative to the spacecraft hub, and the second prescribes 1-DOF rotational motion relative to the hub. Cubic splines are used to implement a smoothed bang-coast-bang acceleration profile for both types of motion.

The value that these simple profiler modules contribute to this body of work cannot be understated. A wide plethora of subcomponent motion and simulation capability is unlocked using these

Table 1 Numerical simulation parameters

Parameter	Notation	Value	Unit
Number of elements per solar array	N	10	N/A
Total spacecraft mass	m_{sc}	900.0	kg
Hub mass	m_{hub}	800.0	kg
Array element mass	m_P	5.0	kg
Hub inertia matrix about hub center of mass	${}^{\mathcal{B}}[I_{\text{hub},B_c}]$	$\begin{bmatrix} 1333.33 & 0.0 & 0.0 \\ 0.0 & 1333.33 & 0.0 \\ 0.0 & 0.0 & 533.33 \end{bmatrix}$	$\text{kg} \cdot \text{m}^2$
Array element inertia matrix about element center of mass	${}^{\mathcal{F}}[I_{P,F_c}]$	$\begin{bmatrix} 6.67 & 0.0 & 0.0 \\ 0.0 & 9.21 & 0.0 \\ 0.0 & 0.0 & 2.55 \end{bmatrix}$	$\text{kg} \cdot \text{m}^2$
Hub center of mass location w.r.t. point B	${}^{\mathcal{B}}\boldsymbol{r}_{B_c/B}$	[0.0, 0.0, 0.0]	m
Array 1 mount frame location w.r.t. point B	${}^{\mathcal{B}}\boldsymbol{r}_{M_1/B}$	[2.0, 0.0, 0.0]	m
Array 2 mount frame location w.r.t. point B	${}^{\mathcal{B}}\boldsymbol{r}_{M_2/B}$	[−2.0, 0.0, 0.0]	m
Array radius	R	4.0	m
Element ij frame location w.r.t. point M_i (init. dep.)	${}^{\mathcal{M}_i}\boldsymbol{r}_{F_{ij}/M_i}$	[0.0, 0.0, 0.0]	m
Element ij frame location w.r.t. point M_i (main dep.)	${}^{\mathcal{M}_i}\boldsymbol{r}_{F_{ij}/M_i}$	$(-1)^{i+1}$ [4.0, 0.0, 0.0]	m

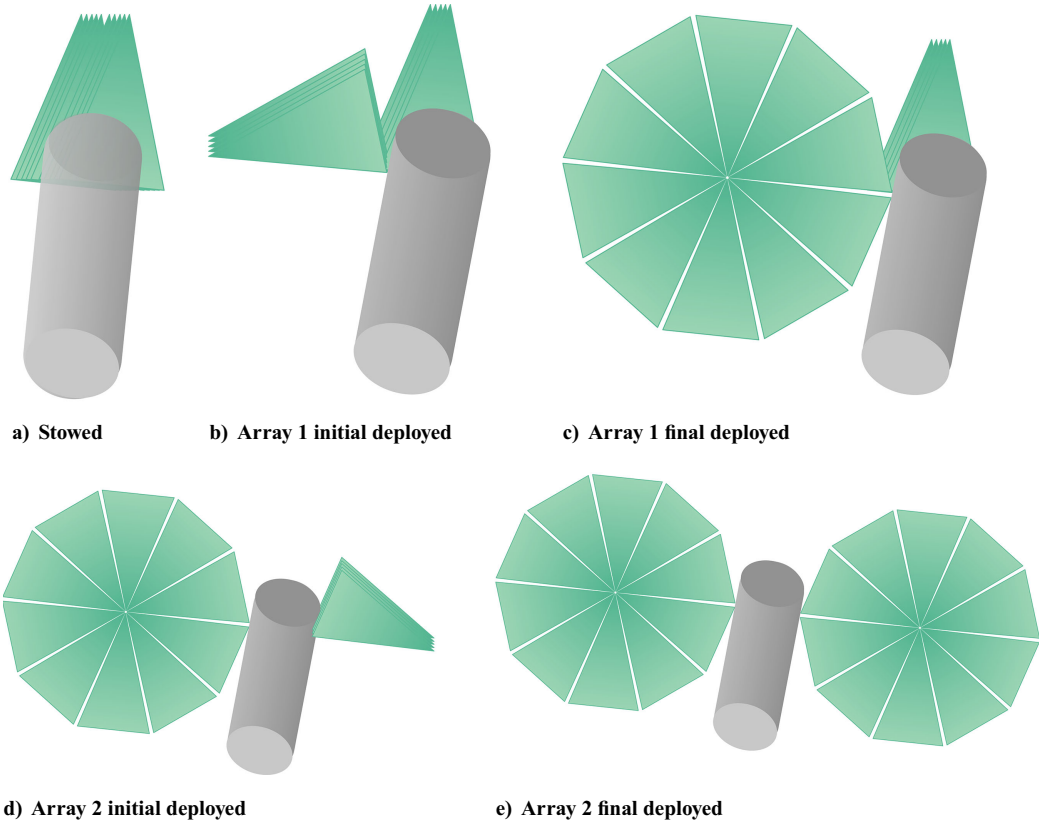

a) Stowed **b) Array 1 initial deployed** **c) Array 1 final deployed**

d) Array 2 initial deployed **e) Array 2 final deployed**

Fig. 2 Solar array configurations for the rotational deployment scenarios.

simple profilers. For example, multibody actuated spacecraft components such as robotic arms or deploying solar arrays can be broken down into prescribed subcomponents moving relative to the spacecraft hub. Both the telescoping and rotational motion of these multibody spacecraft components can be simulated with these simple profiler modules. Further, these profiler modules can be used for verification of the developed hub equations of motion. This verification is provided in Appendix B of this work.

Table 2 lists the inputs required to profile the rotational subcomponent motion. ${}^{\mathcal{M}}\hat{\boldsymbol{s}}$ is the subcomponent axis of rotation expressed as a unit vector in mount frame components; θ_0 and θ_{ref} are the initial and final subcomponent rotation angles relative to the hub, respectively; $\ddot{\theta}_{\max}$ is the maximum angular acceleration used during the bang segments of the rotation. Δt_{bang} is the duration the maximum acceleration is applied during each bang segment, while Δt_{smooth} is the time the acceleration is smoothed before and after each bang segment to ensure that the acceleration profile is continuous across the entire rotation. Using these inputs, the subcomponent's hub-relative scalar states $\theta(t)$, $\dot{\theta}(t)$, and $\ddot{\theta}(t)$ are determined as a function of time.

Table 3 lists the inputs required to profile the translational subcomponent motion. ${}^{\mathcal{M}}\hat{\boldsymbol{\rho}}$ is the subcomponent axis of translation expressed as a unit vector in mount frame components; ρ_0 and ρ_{ref} are the initial and final subcomponent displacements relative

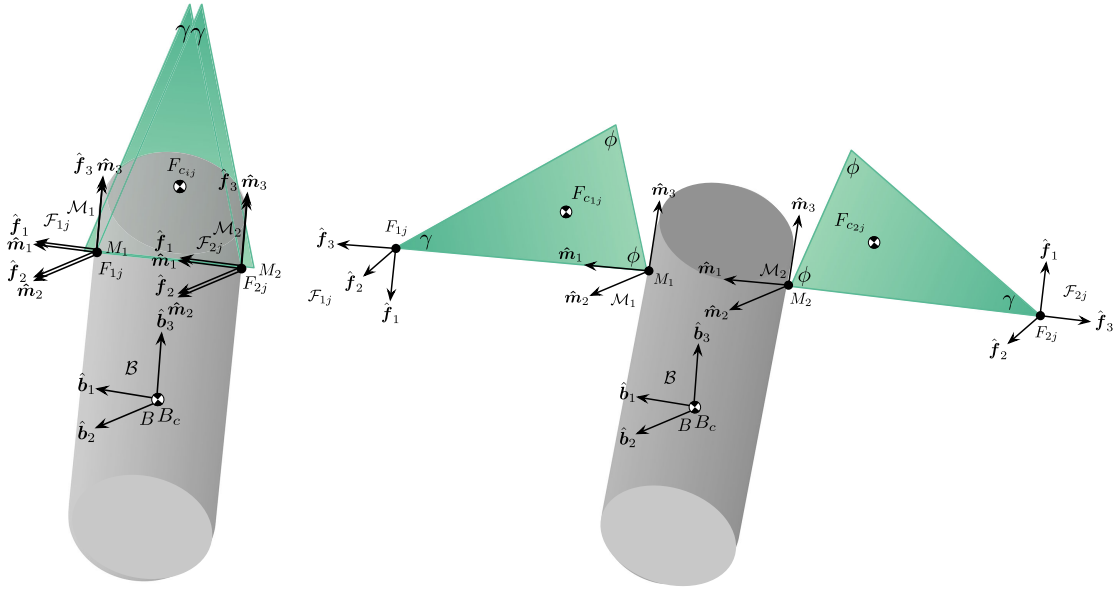

a) Stowed configuration b) Initial deployed configuration

Fig. 3 Rotational deployment scenario frame definitions.

Table 2 Rotational profiler input parameters

Parameter	Notation	Unit
Subcomponent rotation axis	${}^{\mathcal{M}}\hat{\boldsymbol{s}}$	N/A
Initial subcomponent angle	θ_0	rad
Reference subcomponent angle	θ_{ref}	rad
Maximum angular acceleration	$\ddot{\theta}_{\text{max}}$	rad/s^2
Duration acceleration segments are applied	Δt_{bang}	s
Acceleration smoothing duration	Δt_{smooth}	s

Table 3 Translational profiler input parameters

Parameter	Notation	Unit
Subcomponent translational axis	${}^{\mathcal{M}}\hat{\boldsymbol{\rho}}$	N/A
Initial subcomponent displacement	ρ_0	m
Reference subcomponent displacement	ρ_{ref}	m
Maximum translational acceleration	$\ddot{\rho}_{\text{max}}$	m/s^2
Duration acceleration segments are applied	Δt_{bang}	s
Acceleration smoothing duration	Δt_{smooth}	s

to the hub, respectively; $\ddot{\rho}_{\text{max}}$ is the maximum linear acceleration used during the bang segments of the translation. Similar to the rotational motion profiler module, Δt_{bang} is the duration the maximum acceleration is applied during each bang segment, while Δt_{smooth} is the time the acceleration is smoothed before and after each bang segment to ensure the acceleration profile is continuous across the entire translation. Using these inputs, the subcomponent's hub-relative scalar states $\rho(t), \dot{\rho}(t)$, and $\ddot{\rho}(t)$ are determined as a function of time.

The mathematics used to develop the kinematic profiler modules is discussed in Appendix A. The equations required to profile both types of motion are identical, so only the equations used to profile the rotational motion are provided in the Appendix. Note that these profiler modules do not implicitly consider constraints such as the actuator displacement, rate, or jerk; however, the user can select input parameters to comply with such constraints without difficulty. Moreover, these modules can be readily augmented or entirely replaced by other formulations in order to address these constraints.

For the deployment-specific scenario studied in this work, it should be noted that only the array elements' rotational motion must be specifically profiled during each phase of array deployment. Each element's translational motion can be considered fixed relative to the hub during each phase of the deployment if the array element translational positions are adjusted upon completion of the initial deployment phase, as seen in Table 1. By shifting the array element displacements relative to the hub before the main deployment phase, only the rotational motion of the array elements must be profiled. The initial and final displacements for the translational profilers are accordingly set to be identical for each phase of the array deployment such that the translational states are fixed throughout each phase of deployment. The deployment-specific rotational profiler parameters are given in Table 4.

Table 4 Deployment scenario-specific rotational profiler input parameters

Parameter	Notation	Value	Unit
Acceleration segment duration	Δt_{bang}	2.0	s
Smoothing segment duration	Δt_{smooth}	2.0	s
Array element rotational axis	${}^{\mathcal{M}}\hat{\boldsymbol{s}}$	[0.0, 1.0, 0.0]	N/A
Element ij initial angle (init. dep.)	$\theta_{ij,0}$	0.0	deg
Element ij reference angle (init. dep.)	$\theta_{ij,\text{ref}}$	$(-1)^{i+1}$ 108.0	deg
Element ij max. accel. (init. dep.)	$\ddot{\theta}_{\text{max}_{ij}}$	0.091	deg /s^2
Element ij initial angle (main dep.)	$\theta_{ij,0}$	$(-1)^{i+1}$ 108.0	deg
Element ij reference angle (main dep.)	$\theta_{ij,\text{ref}}$	$36j + (-1)^{i+1}$ 108.0	deg
Element ij max. accel. (main dep.)	$\ddot{\theta}_{\text{max}_{ij}}$	(j-1) 7.519e-3	deg /s^2

C. Results

The results for this simulated scenario can be seen in Figs. 4 and 5. The profiled array element states throughout the deployment simulation are presented in Fig. 4, while the hub inertial response to the array deployment is provided in Fig. 5.

Viewing Fig. 4a, array 1 is first seen to rotate by +108 deg during the initial deployment phase to bring the array elements from the stowed configuration to the initially deployed configuration. After this initial rotation, all array 1 elements are seen to begin

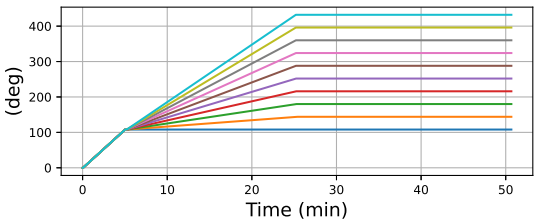

a) Array 1 angle $\theta_1(t)$

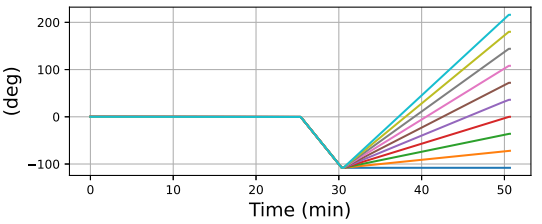

b) Array 2 angle $\theta_2(t)$

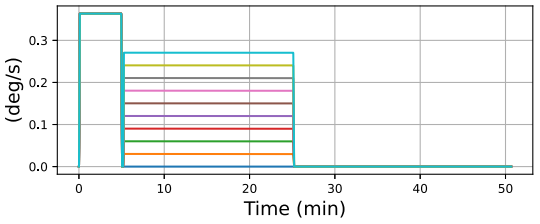

c) Array 1 angle rate $\dot{\theta}_1(t)$

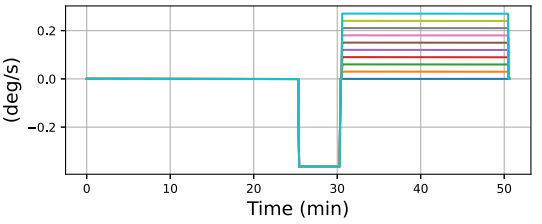

d) Array 2 angle rate $\dot{\theta}_2(t)$

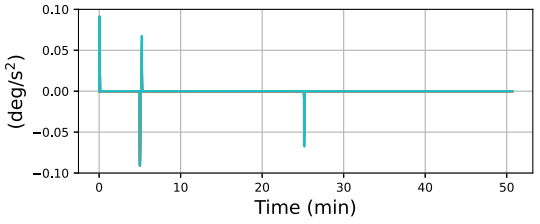

e) Array 1 angular acceleration $\ddot{\theta}_1(t)$

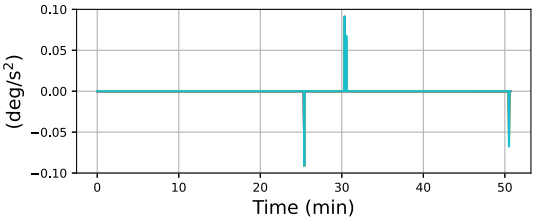

f) Array 2 angular acceleration $\ddot{\theta}_2(t)$

Fig. 4 Profiled array element states for the deployment scenario.

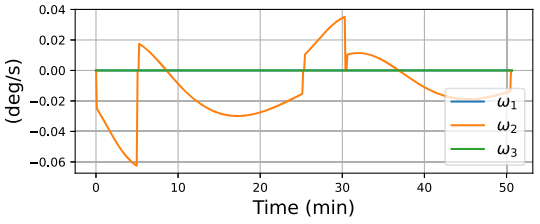

a) Hub inertial angular velocity ${}^{\mathcal{B}}\omega_{\mathcal{B}/\mathcal{N}}$

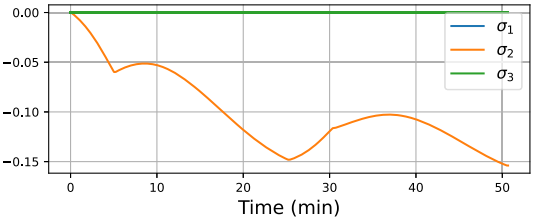

b) Hub inertial attitude $\sigma_{\mathcal{B}/\mathcal{N}}$

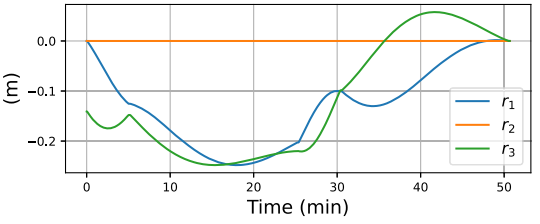

c) Hub inertial position ${}^{\mathcal{N}}r_{B/N}$

Fig. 5 Hub dynamic response throughout the deployment scenario.

the main deployment phase and rotate together with different acceleration profiles in order to lock into their final deployed configurations simultaneously. Figure 4c illustrates array 2 deploying with symmetric behavior after array 1 fully completes its deployment. The acceleration profiles used to prescribe the array deployments are seen in Figs. 4e and 4f. These smoothed bang-coast-bang acceleration profiles produce the angular rate plots seen in Figs. 4c and 4d.

Figure 5a presents the hub inertial angular velocity during the array deployment. The hub rate about the $\hat{\boldsymbol{b}}_2$ axis varies with a maximum value occurring after array 1 completes the initial deployment phase. The hub rates about the $\hat{\boldsymbol{b}}_1$ and $\hat{\boldsymbol{b}}_3$ axes are seen to remain near zero throughout the entire deployment. During the main deployment phases, the second hub angular velocity component compensates for the motion of the array elements by fluctuating smoothly between roughly ± 0.02 and ± 0.01 deg/s. This behavior is expected, as the hub must respond to conserve the total spacecraft angular momentum about its center of mass. Considering Figs. 5b and 5c, the hub inertial attitude and position are seen to shift appropriately during each phase of deployment. During the deployment of array 1 in the X-Z hub frame plane, the hub compensates by both translating and rotating negatively in the inertial X-Z plane. During the deployment of array 2 in the X-Z hub plane, the hub

appropriately translates and rotates positively in the inertial X-Z plane. Note that the initial hub attitude is aligned with the inertial reference frame.

VI. Conclusions

The ability to extensively simulate complex space vehicles before mission launch is crucial for mission success. With the growing complexity of appendages attached to the central spacecraft hub, such as deploying articulable solar arrays and multilink robotic manipulator arms, accurately modeling the dynamics of these complex structures and analyzing their impact on the spacecraft hub dynamics becomes increasingly more valuable to ensure confidence and reliability in the selected spacecraft design.

This work develops a generalized multibody dynamics formulation to simulate a spacecraft consisting of a rigid hub with N-element prescribed motion components that actuate relative to the spacecraft hub. The solution yields a modular way to simulate a spacecraft whose subcomponent motion is kinematically prescribed. The developed formulation is novel in that the current spacecraft dynamics software simulation capability is expanded to enable a modular, reconfigurable, and efficient implementation of any complex spacecraft design containing prescribed motion elements.

The derived dynamics are implemented in the Basilisk astrodynamics simulation software framework and verified by demonstrating that the quantities of orbital angular momentum, orbital energy, and rotational angular momentum are indeed preserved in a conservative environment. The scalability of the developed dynamics is demonstrated using a prescribed motion solar array deployment scenario. The dynamic impact of the prescribed solar array deployment on the overall spacecraft hub motion is studied. The development of these general software tools enables a more accessible, rapid approach to simulating and analyzing complex time-varying spacecraft geometries.

Appendix A: Kinematic Profiler Mathematics

This section discusses the mathematics used to develop the prescribed translational and rotational kinematic profiler modules. Note that the equations required to profile both types of motion are identical, so only the equations used to profile the rotational motion are provided here. The rotational motion is split into seven distinct segments. The first segment of the rotation smooths the acceleration from zero to the specified maximum angular acceleration value $\ddot{\theta}_{\max}$ in the given time Δt_{smooth}. If the given reference angle is greater than the initial angle, the acceleration is smoothed positively to the given maximum acceleration value. If the given reference angle is less than the initial angle, the acceleration is smoothed from zero to the negative maximum acceleration value. During this phase, the scalar hub-relative states of the subcomponent are as follows:

Segment 1: $t_0 \le t \le t_{s_1}$

$$\ddot{\theta}(t) = \pm\ddot{\theta}_{\max}\left(\frac{3(t-t_0)^2}{\Delta t_{\text{smooth}}^2} - \frac{2(t-t_0)^3}{\Delta t_{\text{smooth}}^3}\right) \tag{A1a}$$

$$\dot{\theta}(t) = \pm\ddot{\theta}_{\max}\left(\frac{(t-t_0)^3}{\Delta t_{\text{smooth}}^2} - \frac{(t-t_0)^4}{2\Delta t_{\text{smooth}}^3}\right) \tag{A1b}$$

$$\theta(t) = \pm\ddot{\theta}_{\max}\left(\frac{(t-t_0)^4}{4\Delta t_{\text{smooth}}^2} - \frac{(t-t_0)^5}{10\Delta t_{\text{smooth}}^3}\right) + \theta_0 \tag{A1c}$$

where

$$t_{s_1} = t_0 + \Delta t_{\text{smooth}} \tag{A2}$$

The second segment of the rotation is the first bang segment, where the maximum acceleration value is applied positively if the reference angle is greater than the initial angle and negatively if the reference angle is less than the initial angle. The subcomponent states during this phase are as follows:

Segment 2: $t_{s_1} < t \le t_{b_1}$

$$\ddot{\theta}(t) = \pm\ddot{\theta}_{\max} \tag{A3a}$$

$$\dot{\theta}(t) = \pm\ddot{\theta}_{\max}(t - t_{s_1}) + \dot{\theta}(t_{s_1}) \tag{A3b}$$

$$\theta(t) = \pm\frac{\ddot{\theta}_{\max}(t-t_{s_1})^2}{2} + \dot{\theta}(t_{s_1})(t-t_{s_1}) + \theta(t_{s_1}) \tag{A3c}$$

where

$$t_{b_1} = t_{s_1} + \Delta t_{\text{bang}} \tag{A4}$$

During the third segment of the rotation, the acceleration is smoothed as it returns to zero. The profiled states during this phase are as follows:

Segment 3: $t_{b_1} < t \le t_{s_2}$

$$\ddot{\theta}(t) = \ddot{\theta}_{\max}\left(1 - \frac{3(t-t_{b_1})^2}{\Delta t_{\text{smooth}}^2} - \frac{2(t-t_{b_1})^3}{\Delta t_{\text{smooth}}^3}\right) \tag{A5a}$$

$$\dot{\theta}(t) = \ddot{\theta}_{\max}\left((t-t_{b_1}) - \frac{(t-t_{b_1})^3}{\Delta t_{\text{smooth}}^2} - \frac{(t-t_{b_1})^4}{2\Delta t_{\text{smooth}}^3}\right) + \dot{\theta}(t_{b_1}) \tag{A5b}$$

$$\theta(t) = \ddot{\theta}_{\max}\left(\frac{(t-t_{b_1})^2}{2} - \frac{(t-t_{b_1})^4}{4\Delta t_{\text{smooth}}^2} - \frac{(t-t_{b_1})^5}{10\Delta t_{\text{smooth}}^3}\right) + \dot{\theta}(t_{b_1})(t-t_{b_1}) + \theta(t_{b_1}) \tag{A5c}$$

where

$$t_{s_2} = t_{b_1} + \Delta t_{\text{smooth}} \tag{A6}$$

The fourth segment of the rotation is the coast segment, where the profiled acceleration is held constant at zero. The subcomponent states are profiled using the following equations:

Segment 4: $t_{s_2} < t \le t_c$

$$\ddot{\theta}(t) = 0 \tag{A7a}$$

$$\dot{\theta}(t) = \dot{\theta}(t_{s_2}) \tag{A7b}$$

$$\theta(t) = \dot{\theta}(t_{s_2})(t - t_{s_2}) + \theta(t_{s_2}) \tag{A7c}$$

where

$$t_c = t_{s_2} + \Delta t_{\text{coast}} \tag{A8}$$

The duration of the coast segment, Δt_{coast} is determined using the parameters Δt_{bang} and Δt_{smooth}:

$$\Delta t_{\text{coast}} = \frac{\Delta\theta_{\text{coast}}}{\dot{\theta}(t_{s_2})} \tag{A9}$$

where

$$\Delta\theta_{\text{coast}} = \theta_{\text{ref}} + \theta_0 - 2\theta(t_{s_2}) \tag{A10}$$

The fifth segment smooths the acceleration from zero to the maximum acceleration value before the second bang segment. Opposite to the first segment of the rotation, the acceleration is instead smoothed positively if the reference angle is less than the initial angle and negatively if the reference angle is greater than

the initial angle. The rotational states during this phase are as follows:

Segment 5: $t_c < t \leq t_{s_3}$

$$\ddot{\theta}(t) = \mp\ddot{\theta}_{\max}\left(\frac{3(t-t_c)^2}{\Delta t_{\text{smooth}}^2} - \frac{2(t-t_c)^3}{\Delta t_{\text{smooth}}^3}\right) \tag{A11a}$$

$$\dot{\theta}(t) = \mp\ddot{\theta}_{\max}\left(\frac{(t-t_c)^3}{\Delta t_{\text{smooth}}^2} - \frac{(t-t_c)^4}{2\Delta t_{\text{smooth}}^3}\right) + \dot{\theta}(t_c) \tag{A11b}$$

$$\theta(t) = \mp\ddot{\theta}_{\max}\left(\frac{(t-t_c)^4}{4\Delta t_{\text{smooth}}^2} - \frac{(t-t_c)^5}{10\Delta t_{\text{smooth}}^3}\right) + \dot{\theta}(t_c)(t-t_c) + \theta(t_c) \tag{A11c}$$

where

$$t_{s_3} = t_c + \Delta t_{\text{smooth}} \tag{A12}$$

The sixth segment of the rotation is the second bang segment, where the profiled acceleration is held constant for the duration Δt_{bang}. Recall that the profiled acceleration is positive in this phase if the reference angle is less than the initial angle and negative if the reference angle is greater than the initial angle. The hub-relative states during this phase are as follows:

Segment 6: $t_{s_3} < t \leq t_{b_2}$

$$\ddot{\theta}(t) = \mp\ddot{\theta}_{\max} \tag{A13a}$$

$$\dot{\theta}(t) = \mp\ddot{\theta}_{\max}(t-t_{s_3}) + \dot{\theta}(t_{s_3}) \tag{A13b}$$

$$\theta(t) = \mp\frac{\ddot{\theta}_{\max}(t-t_{s_3})^2}{2} + \dot{\theta}(t_{s_3})(t-t_{s_3}) + \theta(t_{s_3}) \tag{A13c}$$

where

$$t_{b_2} = t_{s_3} + \Delta t_{\text{bang}} \tag{A14}$$

The seventh segment of the rotation is the fourth and final smoothing segment, where the acceleration returns to zero. At the end of this phase, the profiled rotation is complete. The subcomponent rates return to zero, and the hub-relative angle converges to the reference value θ_{ref}. The subcomponent states during this phase are as follows:

Segment 7: $t_{b_2} < t \leq t_f$

$$\ddot{\theta}(t) = \mp\ddot{\theta}_{\max}\left(\frac{3(t_f-t)^2}{\Delta t_{\text{smooth}}^2} - \frac{2(t_f-t)^3}{\Delta t_{\text{smooth}}^3}\right) \tag{A15a}$$

$$\dot{\theta}(t) = \pm\ddot{\theta}_{\max}\left(\frac{(t_f-t)^3}{\Delta t_{\text{smooth}}^2} - \frac{(t_f-t)^4}{2\Delta t_{\text{smooth}}^3}\right) \tag{A15b}$$

$$\theta(t) = \mp\ddot{\theta}_{\max}\left(\frac{(t_f-t)^4}{4\Delta t_{\text{smooth}}^2} - \frac{(t_f-t)^5}{10\Delta t_{\text{smooth}}^3}\right) + \theta_{\text{ref}} \tag{A15c}$$

where

$$t_f = t_{b_2} + \Delta t_{\text{smooth}} \tag{A16}$$

Appendix B: Dynamics Verification

Although numerical simulations may appear to yield appropriate results for a given dynamics formulation, a verification approach is necessary in order to draw meaningful conclusions regarding obtained simulation results. It is difficult to guarantee with certainty that a numerical simulation is without error; however, using a respected verification approach greatly increases confidence in conclusions drawn from obtained results. In order to verify the derived multibody prescribed motion dynamics, the quantities of orbital angular momentum, orbital energy, and spacecraft rotational angular momentum are checked for conservation. The orbital quantities describe the movement of the spacecraft's center of mass in orbit, and the rotational quantities describe the rotation of the spacecraft about its center of mass [21]. Note that the spacecraft rotational energy will not be conserved for the system described in this work because the prescribed accelerations and decelerations add and remove energy from the system, respectively. Therefore, this quantity is checked to ensure it returns to zero at the end of the simulation.

Table B1 Verification scenario parameters

Parameter	Notation	Value	Unit
Total spacecraft mass	m_{sc}	810	kg
Hub mass	m_{hub}	800	kg
Subcomponent mass	m_P	10	kg
Hub inertia matrix about hub center of mass	${}^{\mathcal{B}}[I_{\text{hub},B_c}]$	$\begin{bmatrix} \frac{400}{3} & 0.0 & 0.0 \\ 0.0 & \frac{400}{3} & 0.0 \\ 0.0 & 0.0 & \frac{400}{3} \end{bmatrix}$	$\text{kg} \cdot \text{m}^2$
Subcomponent inertia matrix	${}^{\mathcal{F}}[I_{P,F_c}]$	$\begin{bmatrix} 0.0167 & 0.0 & 0.0 \\ 0.0 & 0.0167 & 0.0 \\ 0.0 & 0.0 & 0.0167 \end{bmatrix}$	$\text{kg} \cdot \text{m}^2$
Hub center of mass location w.r.t. point B	${}^{\mathcal{B}}\boldsymbol{r}_{B_c/B}$	[0.0, 0.0, 0.0]	m
Subcomponent center of mass location w.r.t. point F	${}^{\mathcal{F}}\boldsymbol{r}_{F_c/F}$	[0.0, 0.0, 0.0]	m
Acceleration segment duration	Δt_{bang}	1.0	s
Smoothing segment duration	Δt_{smooth}	1.0	s
Rotational axis	${}^{\mathcal{M}}\hat{\boldsymbol{s}}$	[1.0, 0.0, 0.0]	N/A
Initial angle	θ_0	0.0	deg
Reference angle	θ_{ref}	10.0	deg
Maximum angular acceleration	$\ddot{\theta}_{\max}$	0.5	deg/s^2
Translational axis	${}^{\mathcal{M}}\hat{\boldsymbol{\rho}}$	[1.0, 0.0, 0.0]	N/A
Initial displacement	ρ_0	0.0	m
Reference displacement	ρ_{ref}	10	cm
Maximum translational acceleration	$\ddot{\rho}_{\max}$	0.5	cm/s^2

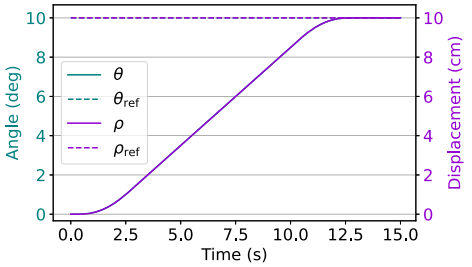

a) Prescribed angle $\theta(t)$ and displacement $\rho(t)$

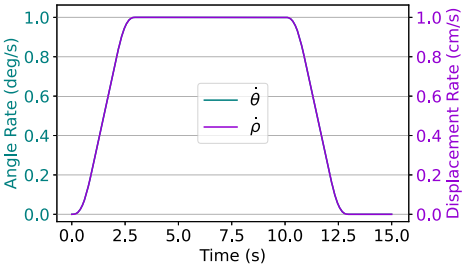

b) Prescribed rates $\dot{\theta}(t)$ and $\dot{\rho}(t)$

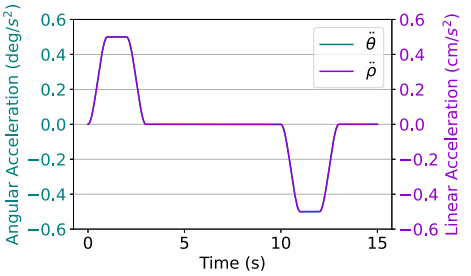

c) Prescribed accelerations $\ddot{\theta}(t)$ and $\ddot{\rho}(t)$

Fig. B1 Prescribed states.

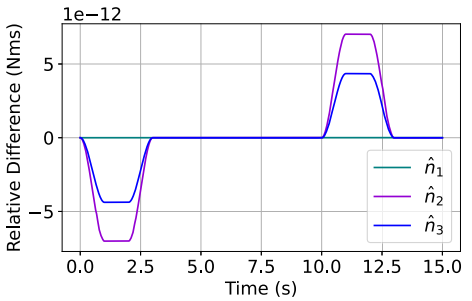

a) Orbital angular momentum

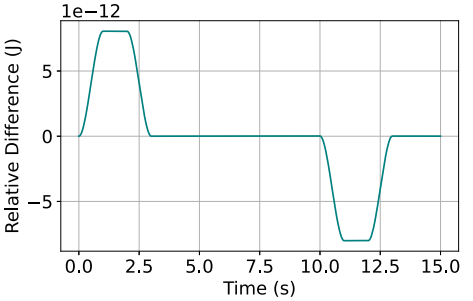

b) Orbital energy

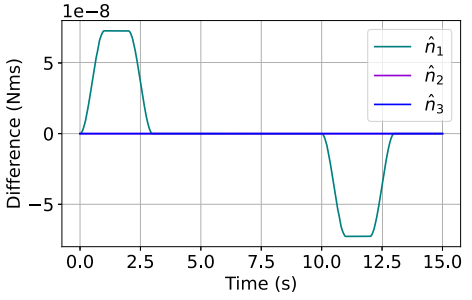

c) Rotational angular momentum

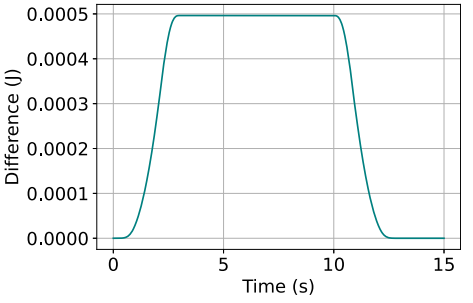

d) Rotational energy

Fig. B2 Verification results.

A rigid hub with a single connected prescribed subcomponent is simulated for the verification scenario. For 15s, the spacecraft is simulated in an inertial orbit in a conservative environment where only gravity is acting on the system. Starting from rest relative to the hub, the subcomponent motion is prescribed to follow simultaneous translation and rotation in order to verify both kinematic profiler modules developed in this work. The subcomponent translates 10 cm along and rotates 10 deg about the hub's first axis $\hat{\boldsymbol{b}}_1$ during the simulation. The simulation parameters chosen for the verification scenario are given in Table B1.

The profiled subcomponent states are shown in Fig. B1. Figure B2 displays the changes in the four quantities of orbital angular momentum, orbital energy, spacecraft rotational angular momentum, and spacecraft rotational energy. Because no nonconservative external forces are acting on the system, the orbital angular momentum, orbital energy, and spacecraft rotational angular momentum are conserved. Figure B2d confirms the expected results for the spacecraft rotational energy, where the spacecraft returns to a state of zero rotational energy at the end of the simulation. The obtained verification results give further confidence in the presented dynamics formulation.

Acknowledgments

Leah Kiner would like to acknowledge João Vaz-Carneiro and Galen Bascom for their fruitful discussions, insights, and comments on the manuscript.

References

[1] Aikenhead, B. A., Daniell, R. G., and Davis, F. M., "Canadarm and the Space Shuttle," *Journal of Vacuum Science and Technology A: Vac-*

uum, Surfaces, and Films, Vol. 1, No. 2, 1983, pp. 126–132. https://doi.org/10.1116/1.572085

[2] Sachdev, S., "Canadarm- a Review of Its Flights," *Journal of Vacuum Science and Technology A: Vacuum, Surfaces, and Films*, Vol. 4, No. 3, 1986, pp. 268–272. https://doi.org/10.1116/1.573952

[3] Gibb, J., "Lightweight Flexible Space Solar Arrays, Past, Present and Future," *2018 IEEE 7th World Conference on Photovoltaic Energy Conversion (WCPEC) (A Joint Conference of 45th IEEE PVSC, 28th PVSEC & 34th EU PVSEC)*, Inst. of Electrical and Electronics Engineers, New York, 2018, pp. 3530–3534. https://doi.org/10.1109/PVSC.2018.8547918

[4] Sun, J., "A New Design of the 3D Deployable Solar Array in the Aerospace Field and Kinematic Analysis During Deployment," *Journal of Physics: Conference Series*, Vol. 2364, No. 1, 2022, Paper 012039. https://doi.org/10.1088/1742-6596/2364/1/012039

[5] Parker, J., Hameli, F., Knittel, J., Caudill, M., Chikine, S., Baskar, S., Koehler, A., and Imler, P., "AAS 24-064 the Preliminary Mission Design of the Emirates Mission to Explore the Asteroids (EMA)," *46th AAS Guidance, Navigation, and Control Conference*, AAS Paper 2024-064, Feb. 2024.

[6] Calaon, R., Allard, C., and Schaub, H., "Solar Electric Propulsion GN&C Pointing State Overview For the Emirates Mission To the Asteroid Belt," *AAS Guidance and Control Conference*, AAS Paper 24-056, Springfield, VA, 2024.

[7] Brophy, J., "NASA's Deep Space 1 Ion Engine (Plenary)," *Review of Scientific Instruments*, Vol. 73, No. 2, 2002, pp. 1071–1078. https://doi.org/10.1063/1.1432470

[8] Brophy, J., Marcucci, M., Ganapathi, G., Garner, C., Henry, M., Nakazono, B., and Noon, D., "The Ion Propulsion System for Dawn," AIAA Paper 2003-4542, 2003. https://doi.org/10.2514/6.2003-4542

[9] Oh, D. Y., Collins, S., Drain, T., Hart, W., Imken, T., Larson, K., Marsh, D., Muthulingam, D., Snyder, J. S., Trofimov, D., et al., "Development of the Psyche Mission for NASA's Discovery Program," *36th International Electric Propulsion Conference*, Paper IEPC-2019-192, Univ. of Vienna, Vienna, Austria, 2019.

[10] Sovey, J. S., Rawlin, V. K., and Patterson, M. J., "Ion Propulsion Development Projects in U.S.: Space Electric Rocket Test I to Deep Space 1," *Journal of Propulsion and Power*, Vol. 17, No. 3, 2001, pp. 517–526. https://doi.org/10.2514/2.5806

[11] Calaon, R., Kiner, L., Allard, C., and Schaub, H., "Momentum Management of a Spacecraft Equipped with a Dual-Gimballed Electric Thruster," *AAS Guidance and Control Conference*, AAS Paper 23-178, Springfield, VA, 2023.

[12] Kiner, L., Allard, C., and Schaub, H., "Two-Axis Gimbal Simulation Overview For the Emirates Mission To the Asteroid Belt," *AAS Guidance, Navigation and Control Conference*, AAS Paper 25-013, Springfield, VA, 2025.

[13] Banerjee, A. K., "Contributions of Multibody Dynamics to Space Flight: A Brief Review," *Journal of Guidance, Control, and Dynamics*, Vol. 26, No. 3, 2003, pp. 385–394. https://doi.org/10.2514/2.5069

[14] Modi, V. J., "Attitude Dynamics of Satellites with Flexible Appendages —A Brief Review," *Journal of Spacecraft and Rockets*, Vol. 11, No. 11, 1974, pp. 743–751. https://doi.org/10.2514/3.62172

[15] Jain, A., "Unified Formulation of Dynamics for Serial Rigid Multibody System," *Journal of Guidance, Control, and Dynamics*, Vol. 14, No. 3, 1991, pp. 531–542. https://doi.org/10.2514/3.20672

[16] Pradhan, S., Modi, V. J., and Misra, A. K., "Order N Formulation for Flexible Multibody Systems in Tree Topology: Lagrangian Approach," *Journal of Guidance, Control, and Dynamics*, Vol. 20, No. 4, 1997, pp. 665–672. https://doi.org/10.2514/2.4129

[17] Anderson, K., "An Order N Formulation for the Motion Simulation of General Multi-Rigid-Body Tree Systems," *Computers & Structures*, Vol. 46, No. 3, 1993, pp. 547–559. https://doi.org/10.1016/0045-7949(93)90224-2

[18] Critchley, J., and Anderson, K. S., "A Generalized Recursive Coordinate Reduction Method for Multibody System Dynamics," *International Journal for Multiscale Computational Engineering*, Vol. 1, Nos. 2–3, 2003, p. 20. https://doi.org/10.1615/IntJMultCompEng.v1.i23.50

[19] Allard, C., Schaub, H., and Piggott, S., "General Hinged Rigid-Body Dynamics Approximating First-Order Spacecraft Solar Panel Flexing," *Journal of Spacecraft and Rockets*, Vol. 55, No. 5, 2018, pp. 1290–1298. https://doi.org/10.2514/1.A34125

[20] Johnston, J. D., and Thornton, E. A., "Thermally Induced Attitude Dynamics of a Spacecraft with a Flexible Appendage," *Journal of Guidance, Control, and Dynamics*, Vol. 21, No. 4, 1998, pp. 581–587. https://doi.org/10.2514/2.4297

[21] Allard, C., Ramos, M. D., Schaub, H., Kenneally, P., and Piggott, S., "Modular Software Architecture for Fully Coupled Spacecraft Simulations," *Journal of Aerospace Information Systems*, Vol. 15, No. 12, 2018, pp. 670–683. https://doi.org/10.2514/1.I010653

[22] Kenneally, P. W., Piggott, S., and Schaub, H., "Basilisk: A Flexible, Scalable and Modular Astrodynamics Simulation Framework," *Journal of Aerospace Information Systems*, Vol. 17, No. 9, 2020, pp. 496–507. https://doi.org/10.2514/1.I010762

[23] Allard, C., Diaz Ramos, M., and Schaub, H., "Computational Performance of Complex Spacecraft Simulations Using Back-Substitution," *Journal of Aerospace Information Systems*, Vol. 16, No. 10, 2019, pp. 427–436. https://doi.org/10.2514/1.I010713

[24] Allard, C., Diaz-Ramos, M., and Schaub, H., "Spacecraft Dynamics Integrating Hinged Solar Panels and Lumped-Mass Fuel Slosh Model," *AIAA/AAS Astrodynamics Specialist Conference*, AIAA Paper 2016-5684, 2016. https://doi.org/10.2514/6.2016-5684

[25] Alcorn, J., Allard, C., and Schaub, H., "Fully Coupled Reaction Wheel Static and Dynamic Imbalance for Spacecraft Jitter Modeling," *AIAA Journal of Guidance, Control, and Dynamics*, Vol. 41, No. 6, 2018, pp. 1380–1388. https://doi.org/10.2514/1.G003277

[26] Alcorn, J., Allard, C., and Schaub, H., "Fully-Coupled Dynamical Jitter Modeling of Variable-Speed Control Moment Gyroscopes," *AAS/AIAA Astrodynamics Specialist Conference*, AAS Paper 17-730, Springfield, VA, 2017.

[27] Vaz Carneiro, J., Allard, C., and Schaub, H., "General Dynamics for Single- and Dual-Axis Rotating Rigid Spacecraft Components," *Journal of Spacecraft and Rockets*, Vol. 61, No. 4, 2024, pp. 1099–1113. https://doi.org/10.2514/1.A35865

[28] Vaz Carneiro, J., Allard, C., and Schaub, H., "Rotating Rigid Body Dynamics Architecture For Spacecraft Simulation Software Implementation," *AAS Guidance and Control Conference*, AAS Paper 23-112, Springfield, VA, 2023.

[29] Vaz Carneiro, J., Johnson, P., and Schaub, H., "Backsubstitution Method for Spacecraft with Generally Translating Appendages," *AAS Astrodynamics Specialist Conference*, AAS Paper 24-248, Springfield, VA, 2024.

[30] Jain, A., and Rodriguez, G., "Recursive Dynamics Algorithm for Multibody Systems with Prescribed Motion," *Journal of Guidance, Control, and Dynamics*, Vol. 16, No. 5, 1993, pp. 830–837. https://doi.org/10.2514/3.21089

[31] Mcgregor, R., and Oshinowo, L., "Flight 6A: Deployment and Checkout of the Space Station Remote Manipulator System (SSRMS)," *6th International Symposium on Artificial Intelligence and Robotics and Automation in Space: i-SAIRAS*, Canadian Space Agency, St-Hubert, Quebec, Canada, June 2001.

[32] Ardakani, H. A., and Bridges, T., "Dynamic Coupling Between Shallow-Water Sloshing and a Vehicle Undergoing Planar Rigid-Body Motion," Tech. Rept., Dept. of Mathematics, Univ. of Surrey, May 2010.

[33] Gerrits, J., and Veldman, A., "Dynamics of Liquid-Filled Spacecraft," *Journal of Engineering Mathematics*, Vol. 45, No. 1, 2003, pp. 21–38. https://doi.org/10.1023/A:1022055916067

[34] Veldman, A., Gerrits, J., Luppes, R., Helder, J., and Vreeburg, J., "The Numerical Simulation of Liquid Sloshing on Board Spacecraft," *Journal of Computational Physics*, Vol. 224, No. 1, 2007, pp. 82–99. https://doi.org/10.1016/j.jcp.2006.12.020

[35] "POEMS: Parallelizable Open-Source Efficient Multibody Software," *Engineering with Computers*, Vol. 23, No. 1, 2007, pp. 11–23. https://doi.org/10.1007/s00366-006-0026-x

[36] Schaub, H., and Junkins, J. L., *Analytical Mechanics of Space Systems*, 4th ed., AIAA Education Series, AIAA, Reston, VA, 2018.

[37] Sidi, M. J., *Spacecraft Dynamics and Control: A Practical Engineering Approach*, Vol. 7, Cambridge Univ. Press, New York, 1997, pp. 291–298, Chap. 10.

[38] Allard, C., Maxwell, J., and Schaub, H., "A Transport Theorem for the Inertia Tensor for Simplified Spacecraft Dynamics Development," *International Astronautical Congress*, Paris, France, 2022.

T. McLain
Associate Editor